



CHALMERS
UNIVERSITY OF TECHNOLOGY

Cobalt- and Nickel-Doped WSe₂ as Efficient Electrocatalysts for Water Splitting and as Cathodes in Hydrogen Evolution Reaction

Downloaded from: <https://research.chalmers.se>, 2025-04-04 12:35 UTC

Citation for the original published paper (version of record):

Kagkoura, A., Canto-Aguilar, E., Gracia-Espino, E. et al (2025). Cobalt- and Nickel-Doped WSe₂ as Efficient Electrocatalysts for Water Splitting and as Cathodes in Hydrogen Evolution Reaction Proton Exchange Membrane Water Electrolysis. *Journal of Physical Chemistry C*, 129(6): 2893-2903. <http://dx.doi.org/10.1021/acs.jpcc.4c08163>

N.B. When citing this work, cite the original published paper.

Cobalt- and Nickel-Doped WSe_2 as Efficient Electrocatalysts for Water Splitting and as Cathodes in Hydrogen Evolution Reaction Proton Exchange Membrane Water Electrolysis

Antonia Kagkoura,* Esdras J. Canto-Aguilar, Eduardo Gracia-Espino, Lunjie Zeng, Eva Olsson, Filipa M. Oliveira, Jan Luxa, and Zdeněk Sofer*

Cite This: *J. Phys. Chem. C* 2025, 129, 2893–2903

Read Online

ACCESS |

Metrics & More

Article Recommendations

Supporting Information

ABSTRACT: Efficient electrocatalysts are vital for advancing sustainable fuel cell technology, and the use of affordable alternatives that enhance the reaction kinetics is key to progress. Although, tungsten diselenide (WSe_2) is promising for electrocatalysis, it is not fully explored, especially in oxygen evolution and in applications such as polymer electrolyte membrane water electrolyzer. In this work, we use a simple approach to dope WSe_2 with cobalt or nickel atoms. Both Co- and Ni- WSe_2 exhibit excellent oxygen evolution reaction activity, with overpotentials of 370 and 400 mV at 10 mA/cm², only 90 and 120 mV higher than those of RuO_2 , respectively. For hydrogen evolution reaction, the materials register low potentials at 10 mA/cm², with -0.20 V and -0.22 V vs RHE for Ni- and Co- WSe_2 , respectively. The effective introduction of heteroatoms causes the retention of coordination vacancies, furnishing active catalytic sites that enhanced electrocatalytic performance, resembling this of noble metals in both activity and charge transfer. Moreover, both doped materials show excellent performance and stability as cathode electrocatalysts in the polymer electrolyte membrane water electrolyzer, with great promise for real-world applications. This study promotes sustainable fuel-cell technology through the development of cost-effective, doped WSe_2 electrocatalysts that improve water splitting and hydrogen production efficiency.



INTRODUCTION

Electrochemical water splitting is an interesting approach to energy storage and/or conversion in a bid to reduce humankind's reliance on ever-depleting fossil fuel resources, therefore tempering extreme consequences of climate change in the process.^{1,2} There are various types of fuel cells, but hydrogen H_2/O_2 fuel cells possess better prospects since they emit absolutely zero carbon into the atmosphere; the byproduct results in the form of water.³ Curiously, the oxygen evolution reaction still remains an enigma. With most of the exact reaction mechanisms not determined and the ideal catalysts that can provide optimum activity and stability, many questions and significant challenges remain upon OER.⁴ Reducing the cost is another challenge still waiting to be realized to make it more marketable. These electrocatalysts, which are crucial for process efficiency, still strongly depend on noble metals: platinum in the case of HER and ruthenium/iridium in the case of OER, wildly adding to the cost barrier and limiting scalability for industrial use.^{3,5} It has, therefore, been more pragmatic to explore alternatives that could allow for wide commercialization. Therefore, any valid alternative is being considered by researchers to develop active, inexpensive,

abundant in the Earth's crust, durable, and scalable electrocatalysts.^{1,6–10}

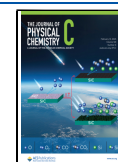
Transition metal dichalcogenides (TMDs) have garnered significant interest for electrocatalytic water splitting, showing promising results.^{6,11–13} Metallic TMDs of the 1T type have naturally lower charge-transfer resistance than their semiconducting 2H counterparts, making them ideal for electrocatalysis.¹⁴ In addition, solvothermal bottom-up approaches provide rich-edged TMDs, which are essential for this purpose.¹⁵ Interestingly, transition metal selenides have received less attention in research compared to the well-studied star, MoS_2 , a typical TMD.^{16–18} Specifically, tungsten diselenide (WSe_2) has been less explored than its molybdenum counterpart, which is somewhat surprising considering that heavier chalcogens typically offer superior electrical con-

Received: December 3, 2024

Revised: January 14, 2025

Accepted: January 17, 2025

Published: January 29, 2025



ductivity—an essential trait for energy-related applications.^{19–21} Although WSe₂-based catalysts have shown notable HER electrocatalytic activity,^{20,22,23} they have only been tested in three-electrode cells, showing great promise as cathode electrocatalysts for Proton exchange membrane (PEM) water electrolysis. However, their performance in these setups cannot be directly applied to real PEM water electrolyzers. The key challenges are (i) the harsh conditions in an actual PEM water electrolyzer (applied potential >1.5 V, low pH), (ii) high operating temperatures, (iii) the use of a solid Nafion membrane as the electrolyte, and (iv) complex heat, water, and gas management issues that are absent in typical electrochemical experiments. Consequently, more research is urgently needed to evaluate WSe₂-based electrocatalysts under realistic PEM water electrolyzer conditions before they can be considered for commercial use. On the other hand, the literature on WSe₂'s electrocatalytic activity in OER is scarce.^{24,25}

Atom incorporation has emerged as an effective approach for improving the electrocatalytic activities of TMDs.²⁶ Atom incorporation mostly takes place at the defect sites within the TMDs.²⁷ Both kinds of heteroatoms, whether metals or nonmetals, will be confined inside the TMDs due to the formation of covalent bonds, which stabilizes atoms in the lattice or coordination environment and leaves hetero- or coordination environments coordinatively unsaturated, thus serving catalytically active sites.²⁸ However, all these doping processes of heteroatoms into TMDs involve sophisticated and high-temperature procedures of chemical vapor deposition;^{27,29} a few of them use simple and low-temperature processes.³⁰ Extensive studies have been carried out on heteroatom doping in MoS₂, while much remains unexplored for WSe₂—only its performance in water splitting, which mostly has not been examined.

Considering all factors above, in this study, we employed a straightforward hydrothermal method to incorporate either cobalt (Co) or nickel (Ni) into WSe₂. The resulting materials, namely, Co–WSe₂ and Ni–WSe₂, demonstrated remarkable electrocatalytic performance for electrocatalytic water splitting, comparable to that of Pt/C and RuO₂ catalysts. Both Co– and Ni–WSe₂ demonstrated high electrocatalytic activity against the OER, resembling this of RuO₂, displaying overpotentials at 10 mA/cm² of just 370 and 400 mV, respectively, only 90 and 120 mV higher than RuO₂. Additionally, both materials showed low potentials against HER at –10 mA/cm², at –0.20 V and –0.22 V vs RHE for Ni– and Co–WSe₂, respectively. Both materials showed low charge transfer resistance and outstanding stability after 10,000 cycles for both electrocatalytic reactions. Additionally, electrocatalysts have been demonstrated to be excellent cathode materials for practical PEM water electrolyzers. The aforementioned results make Co–WSe₂ and Ni–WSe₂ ideal bifunctional electrocatalysts for use in practical PEM water electrolyzers and fuel-cell devices. Our work supports the sustainable advancement of fuel cells and water-splitting technologies by improving reaction kinetics with cost-effective materials.

EXPERIMENTAL SECTION

General. Chemicals, reagents, and solvents were purchased from Sigma-Aldrich and used without further purification.

Raman Spectroscopy. An inVia Raman microscope (Renishaw, England) in backscattering geometry with a CCD detector was used for Raman spectroscopy. DPSS laser (532

nm, 50 mW) with an applied power of 5×mW and 50× magnification objective was used for the measurement. Instrument calibration was achieved with a silicon reference which gives a peak position at 520 cm^{–1} and a resolution of less than 1 cm^{–1}. The samples were suspended in deionized water (1 mg/mL) and ultrasonicated for 10 min. The suspension was deposited on a small piece of silicon wafer and dried.

X-ray Photoelectron Spectroscopy. High-resolution X-ray photoelectron spectroscopy (XPS) was performed using an ESCAProbeP spectrometer (Omicron Nanotechnology Ltd., Germany) with a monochromatic aluminum X-ray radiation source (1486.7 eV). Wide-scan surveys of all elements were performed with subsequent high-resolution scans of the W 4f and Se 3d. The samples were placed on a conductive copper tape. A low energy electron gun was used to eliminate sample charging during the measurement. For survey spectra, an E_{pass} of 50 eV was used while for high-resolution spectra, an E_{pass} of 20 eV was used.

Scanning Electron Microscopy. The morphology was investigated by using scanning electron microscopy (SEM) with a Tescan MAIA-3 field emission gun scanning electron microscope. The samples were placed on carbon conductive tape to conduct the measurements. SEM measurements were carried out by using a 5 kV electron beam.

Transmission Electron Microscopy. A JEOL monochromated ARM200F transmission electron microscopy (TEM) microscope operated at 200 kV was used for scanning transmission electron microscopy (STEM) and STEM–EDS analysis. The TEM microscope was equipped with a CEOS probe aberration corrector, a CEOS image aberration corrector, and a double silicon drift detector for energy-dispersive X-ray spectroscopy (EDS). High-angle annular dark field (HAADF) STEM imaging was used to directly visualize the atomic structure of the crystals. The beam convergence half angle and collection inner half angle are ~27 and 55 mrad, respectively. The resolution for STEM imaging is ~0.8 Å. STEM–EDS was used to map the spatial distribution of elements at the nanometer and atomic scales. TEM specimens were prepared by manually grinding bulk crystals in IPA for 15 min in a mortar. The resultant solution with nanocrystals was drop-cast on a holey carbon-coated Cu grid and dried in air.

Electrochemical Measurements. The electrochemical characterization by means of cyclic linear sweep voltammetry (LSV) was performed using an Autolab PGSTAT 204 instrument (Metrohm, Switzerland). A standard three-compartment electrochemical cell was used equipped with an RDE with a glassy carbon disk (geometric surface area: 0.196 cm²) as a working electrode, platinum as a counter electrode, and Hg/HgSO₄ (0.5 M K₂SO₄) or Hg/HgO (0.1 M KOH) as reference electrodes. HER LSV measurements were performed in N₂-saturated aqueous 0.5 M H₂SO₄ solution and OER LSV measurements or in N₂-saturated aqueous 1.0 M KOH at room temperature. For preparing the catalyst ink, catalytic powder (4.0 mg) was dissolved in a mixture (1 mL) of deionized water, 2-propanol, and 5% Nafion (v/v/v = 4:1:0.02), followed by sonication for 30 min before use. The working electrode was polished with alumina suspension, washed with deionized water, and finally sonicated in double-distilled water before casting 8.5 μL aliquots of the electrocatalytic ink on the electrode's surface. Finally, electrochemical impedance spectroscopy (EIS) measurements were acquired from 10⁵ to 10^{–1} Hz with an AC amplitude of 0.01 V.

Membrane-Electrode Assembly Preparation and Electrochemical Characterization in a Two-Electrode PEM Cell. Membrane-electrode assembly (MEA) devices were prepared by pressing the anode and cathode with a commercial Nafion N-115 polymer electrolyte membrane three times at 130 °C for 2 min using a Stahls Hotronix 6" × 6" heat press. Before the assembly of the device, the membranes were activated by heating them at 80 °C for 1 h in H₂O₂ (3% V/V), deionized water (18.2 MΩ·cm), 0.5 M H₂SO₄, one more time in water, and stored in the same solvent until usage. Both, anode and cathode electrodes, were deposited by the air gun-spraying technique using N₂ as the carrier gas and a high-porosity platinized-Ti fiber felt (at 100 °C) or carbon paper (CP-39BB, at 70 °C) as gas diffusion layers. For the anode, the ink used consisted in an IrO₂ particle dispersion with a concentration of 10.6 mg mL⁻¹ in a solvent mixture of 2-propanol, water, and a Nafion solution (5% wt in ethanol, Nafion D520) in a 84.9:9.7:5.4% V/V ratio; while for the cathode, the catalyst ink consisted in 5.5 mg mL⁻¹ of WSe₂, Ni–WSe₂, Co–WSe₂, or Pt–C (20%, as a reference) dispersed in a 2-propanol/water/Nafion D520 (88.1:10.04:1.86% V/V) mixture. Finally, the electrode's catalyst loading was set to ≈2.5 mg cm⁻² for the anode, ≈0.8 mg cm⁻² for the WSe₂-based cathode catalyst, and ≈0.4 mg cm⁻² of pure Pt for the reference MEA.

The electrochemical performance of freshly prepared MEA devices was evaluated using a Scribner-Electrolyzer test system 600, working at 80 °C and atmospheric pressure conditions, with a feed flow of water at the positive side of 100 mL min⁻¹ and no N₂ flow at the negative side. All MEAs were activated, before any electrochemical characterization, by applying a constant current of 100 mA cm⁻² during 30 min to open channels in the electrocatalytic films for the diffusion of the reaction precursors and increase the release of gases toward the flow fields in the PEM cell. After the activation step, *I*–*V* curves were obtained through galvanostatic step sweep polarization from 40 mA mA to 10 A, at a scan rate of 3 mA per step, a duration of 5 s step, an acquisition time of 5 s per point, and in the potential window of 0.3 to 2.1 V. EIS experiments were performed right after the polarization curves at 0.5 A and an alternant perturbation of 10% in the frequency range of 50 kHz to 0.1 Hz; where the Ohmic resistance (*R*_Ω) and the charge transfer resistance (*R*_{ct}) were calculated by fitting the resulting electrochemical spectra with an equivalent electrical circuit. Finally, information about the stability of the WSe₂-based materials was obtained after keeping the devices at a constant voltage of 1.9 V for 24 h and tracking the changes on the device performance with the polarization curves and EIS characterization at the same conditions as stated above.

Preparation of WSe₂. Tungsten hexacarbonyl (1 mmol) and selenium powder (2 mmol) were dissolved in 30 mL of DMF. The mixture was then placed in a 50 mL Teflon-lined stainless-steel autoclave and heated at 200 °C for 13 h. After cooling to room temperature, the suspension was centrifuged at 10,000 rpm and sequentially washed twice with DMF, three times with water, and three times with methanol.

Preparation of Co–WSe₂. A mixture of 50.6 mg of cobalt acetate tetrahydrate and 36 mg of thiourea was prepared in 1 mL of water and allowed to sit overnight, resulting in the formation of the Co ion complex, Co(thiourea)₄²⁺. Afterward, the solution of the Co thiourea complex was mixed into 50 mL of a stabilized WSe₂ colloid solution (with a concentration of 1 mg mL⁻¹ and containing 30% v/v isopropanol/water with 50

mg of polyvinylpyrrolidone). The resulting dispersion was then transferred to a 100 mL vessel autoclave and subjected to hydrothermal treatment at 160 °C for 24 h.

Preparation of Ni–WSe₂. A mixture consisting 50 mg of nickel acetate tetrahydrate and 36 mg of thiourea was prepared in 1 mL of water and was left overnight to mix, to form the Ni ion complex (Ni(thiourea)₄²⁺). Then, the Ni thiourea complex solution was mixed into 50 mL of a stabilized WSe₂ colloid solution (with a concentration of 1 mg mL⁻¹ and containing 30 v/v % isopropanol/water with 50 mg of polyvinylpyrrolidone). The resulting dispersion was then transferred to a 100 mL vessel autoclave and subjected to hydrothermal treatment at 160 °C for 24 h.

RESULTS AND DISCUSSION

The preparation process of the hybrids involved a straightforward hydrothermal reaction to incorporate single metal atoms (Co or Ni) into 1T/2H–WSe₂, derived from a solvothermal reaction.²⁸ This step involved forming a thiourea–metal complex,²⁸ which selectively occupied the selenium vacancies on the WSe₂ surface due to the high molecular affinity of the defective sites.³¹ The solvothermal reaction followed for the preparation of pristine WSe₂ leads to material with metallic characteristics and flower-like morphology. The latter is confirmed by SEM where images reveal that pristine 1T/2H–WSe₂ and hybrid nanostructures are composed of small, randomly assembled nanosheets that are interconnected, forming intricate 3D flower-like shapes, as illustrated in Figure 1.

XPS and Raman spectroscopy were employed to investigate the doped materials. The deconvoluted W 4f spectrum for pristine 1T/2H–WSe₂ displays two doublets: one corresponding to the 1T phase (31.4 eV for W⁴⁺ 4f_{7/2} and 33.9 eV for W⁴⁺ 4f_{5/2}) and another for the 2H phase (32.35 eV for W⁴⁺ 4f_{7/2} and 34.53 eV for W⁴⁺ 4f_{5/2}), as shown in Figure 2a. Meanwhile, peaks at higher energy levels indicate the presence of W⁶⁺ species within the 1T/2H–WSe₂ structure, which are well known for their beneficial role in enhancing electrocatalytic reactions such as OER and HER.^{32–35} Additionally, the Se 3d spectrum for WSe₂ reveals doublets at 56.0 eV for Se 3d_{3/2} and 55.1 eV for Se 3d_{5/2}, indicating the 2H phase, while energy peaks at 55.0 eV for Se 3d_{3/2} and 54.1 eV for Se 3d_{5/2} correspond to the 1T phase (Figure 2b). In contrast, the doped materials exhibit signals shifted to lower binding energies for W 4f and Se 3d, indicating the presence of electronic interaction between the dopants and WSe₂.³⁶ Specifically, Co–WSe₂ shows peaks at 30.7 eV for W⁴⁺ 4f_{7/2} and 33.5 eV for W⁴⁺ 4f_{5/2} for the 1T phase and 31.9 eV for W⁴⁺ 4f_{7/2} and 34.1 eV for W⁴⁺ 4f_{5/2} for the 2H phase (Figure 2c). Ni–WSe₂ exhibits peaks at 31.2 eV for W⁴⁺ 4f_{7/2} and 33.5 eV for W⁴⁺ 4f_{5/2} for the 1T phase and 32.4 eV for W⁴⁺ 4f_{7/2} and 34.5 eV for W⁴⁺ 4f_{5/2} for the 2H phase (Figure 2e). Meanwhile, Se 3d_{3/2} and Se 3d_{5/2} are downshifted to 55.5 and 54.6 eV (2H) and 54.5 and 53.6 eV (1T), respectively, for Co–WSe₂ and to 55.6 and 54.6 eV (2H) and 54.6 and 53.5 eV (1T) for Ni–WSe₂ materials as seen in Figure 2d,f, respectively. Peaks at around 60.3 eV (Figure 2d) and 67.6 eV (Figure 2f) correspond to Co 3p and Ni 3p, respectively. Additionally, the Co 2p region shows signals at 779.0 eV (Co 2p_{1/2}) and 795.2 eV (Co 2p_{3/2}) as well as two satellite peaks (787.08 and 806.08 eV), which confirm the existence of Co²⁺ (Figure S1a).^{28,37} Similarly, Figure S1b confirms the presence of Ni, showing two main peaks at 873.2 and 855.6 eV corresponding to Ni 2p_{1/2} and 2p_{3/2} spin-orbit

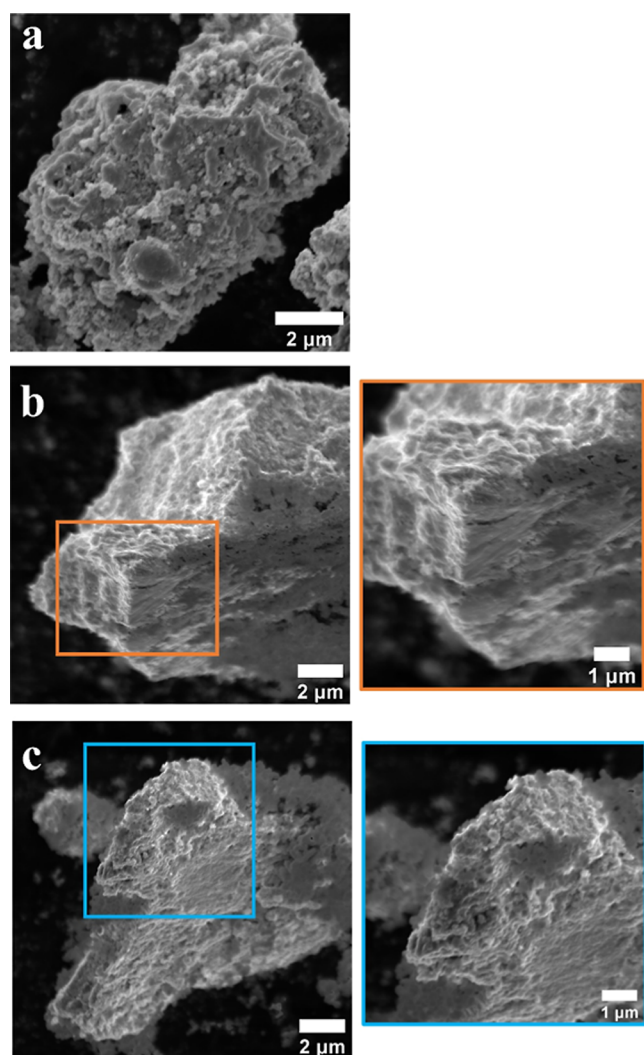


Figure 1. SEM images of (a) pristine 1T/2H-WSe₂, (b) Co-WSe₂, and (c) Ni-WSe₂. Magnifications of (b,c) highlight the layered structure of the materials.

splits along with two satellite peaks.^{38,39} The absence of signals for Co⁰ at ≈ 778.3 eV and Ni⁰ at ≈ 852.6 eV suggests that the formation of Co or Ni clusters is unlikely.⁴⁰ Additional confirmation of the hybrid structure was provided by powder X-ray diffraction analysis. As shown in Figure S2, the reflection peaks correspond to the plane reflections of hexagonal WSe₂ in both doped and pristine 1T/2H-WSe₂ (reference JCPDF no. 38-1388).⁴²

Raman spectroscopy confirmed the presence of the 1T phase in both 1T/2H-WSe₂ and the doped materials (Figure 3). Notably, bands at 128, 202, and 236 cm⁻¹ corresponding to J_1 , J_2 , and J_3 are characteristic phonon modes of the metallic 1T octahedral phase of 1T/2H-WSe₂.⁴¹ Additionally, bands located at 252 cm⁻¹ for WSe₂ result from the overlapping E_{2g}^1 and A_{1g} modes, characteristic of the 2H phase.⁴¹ These bands were blueshifted by 3 cm⁻¹ for the doped materials probably due to the incorporation of Co and/or Ni atoms within 1T/2H-WSe₂.^{25,40,42}

STEM measurements unveiled the nanometer- and atomic-scale structures of Co- and Ni-WSe₂. Consistent with SEM observations, HAADF STEM imaging shows that WSe₂ nanostructures have flower-like morphology (Figure 4a,c,d,g).

This morphology originates from interconnected nanosheets of the crystals in the structures. The distribution of the nanosheets is evident in high-resolution HAADF STEM images (Figure 4e,i,g,k), in which the bright fringes with interfringe distance of ~ 0.65 nm directly show the stacking of the atomic basal planes in the nanosheets. The thickness and length of the nanosheets are around 5 and 10 nm, respectively. It is worth noting that both doped and pristine WSe₂ consist of such randomly distributed nanosheets of WSe₂ crystals. Moreover, STEM-EDS mapping directly revealed the spatial distribution of the dopants in the doped WSe₂ (Figure 4b,d,f,h,j,l). Co and Ni dopants are found to be distributed homogeneously within the WSe₂ crystals. According to EDS analysis, the atomic concentrations of Co and Ni dopants in the doped WSe₂ are $\sim 5\%$ and $\sim 2.5\%$, respectively.

The effectiveness of single-atom-doped WSe₂ electrocatalysts for overall water splitting was investigated. To assess the OER activities, electrodes were prepared by drop-casting the dispersions of Co and Ni-WSe₂ and reference materials 1T/2H-WSe₂ and RuO₂ onto a glassy carbon electrode. LSV was recorded in a N₂-saturated aqueous solution of a 1 M KOH electrolyte (Figure 5a). Remarkably, both doped electrocatalysts displayed excellent performances that reflected the least overpotentials at 10 mA/cm² of 370 mV (1.60 V vs RHE) and 400 mV (1.63 V vs RHE) for Co- and Ni-WSe₂, respectively. These values were only 90 and 120 mV higher than that recorded for RuO₂, which registered 1.51 V vs RHE. In contrast, pristine WSe₂ reflected an overpotential as high as 1320 mV. The above values indicate that the addition of single atoms significantly reduces the overpotential required to generate molecular oxygen. This is due to the confined atoms that maintain coordination vacancies and hence act as catalytically active sites. The strong electronic interaction of the incorporated heteroatoms within 1T/2H-WSe₂ triggers new electronic states, which plays a significant role in the electrocatalytic activity of those sites.²⁸

Tafel slopes were extracted from LSV curves to measure the increase rate of current with applied overpotential. Indeed, Co-doped WSe₂ has the smallest Tafel slope of 45 mV/dec, while RuO₂ and Ni-doped WSe₂ exhibit close values for the Tafel slope at 83 mV/dec. Specifically, the low Tafel slope values are needed for a highly active electrocatalyst; this is because they mean a high OER rate with a steady rise in overpotential, probably favorable in real applications. In sharp contrast, the Tafel slope of pristine WSe₂ was as high as 319 mV/dec, reflecting slower OER kinetics.

EIS assays were conducted to further assess the OER kinetics. EIS measurements were conducted at the potential corresponding to around 2 mA cm⁻² and all data were fitted to a Randles circuit. In the Nyquist plots, both Co- and Ni-WSe₂ displayed a minimal frequency semicircle in the Nyquist plots, indicating a smallest R_{ct} value of 8.23 and 10.19 Ω , respectively (see Figure 5c). In comparison, the R_{ct} value of RuO₂ was 13 Ω , and that of pristine WSe₂ was measured as 50 Ω , which refers to a higher charge transfer resistance. Conversely, the low charge transfer resistance obtained in doped WSe₂ is due to improved conductivity caused by heteroatom doping. The detailed summary of various electrocatalytic OER parameters for Ni- and Co-WSe₂ nanoensembles along with neat 1T/2H-WSe₂ is summarized in Table S1.

The effectiveness of doped WSe₂ electrocatalysts for HER was assessed through LSV in an aqueous 0.5 M H₂SO₄

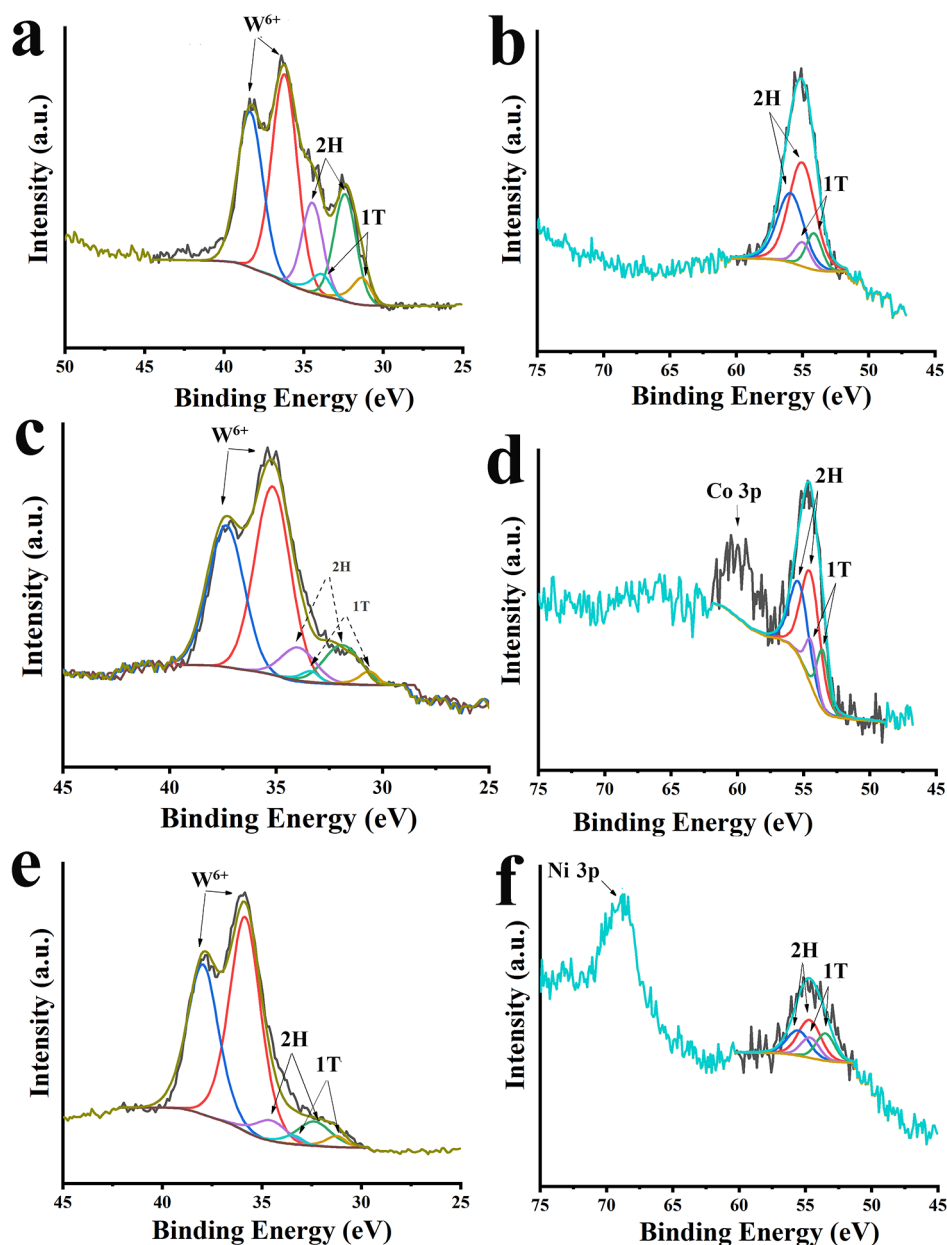


Figure 2. Deconvoluted X-ray photoelectron spectra of (a) W 4f and (b) Se 3d for WS_2 for 1T/2H- WS_2 . (c) W 4f and (d) Se 3d for Co- WS_2 . (e) W 4f and (f) Se 3d for Ni- WS_2 .

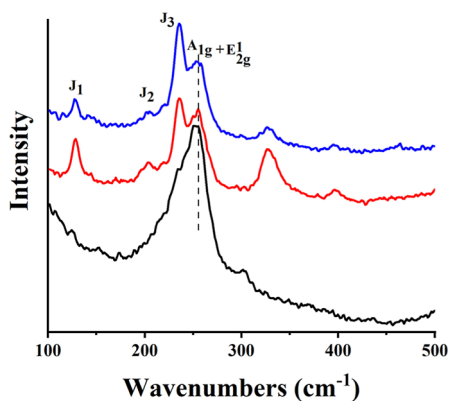


Figure 3. Raman spectra (532 nm) for Co- WS_2 (red), Ni- WS_2 (blue), and 1T/2H- WS_2 (black).

electrolyte. Remarkably, Co-doped and Ni- WS_2 exhibited comparable low onset potentials at -0.15 V vs RHE, nearing Pt/C which registered 0.018 V vs RHE (as depicted in Figure 6a) by 168 mV. Conversely, the undoped WS_2 reference material displayed a higher onset potential at -0.28 V vs RHE (Figure 6a). Furthermore, the electrocatalytic performance of the HER was further examined at -10 mA/cm^2 . Notably, Ni-doped WS_2 and Co-doped 1T/2H- WS_2 were able to catalyze HER at -10 mA/cm^2 at potentials of -0.20 and -0.22 V vs RHE, respectively, approximately 240 and 222 mV lower than that of pristine 1T/2H- WS_2 , which operated at -0.44 V vs RHE. Again, heteroatom integration significantly lowers the overpotential needed for proton reduction to hydrogen by maintaining coordination vacancies that create active catalytic sites. The strong electronic interaction between the incorporated atoms and 1T/2H- WS_2 induces the

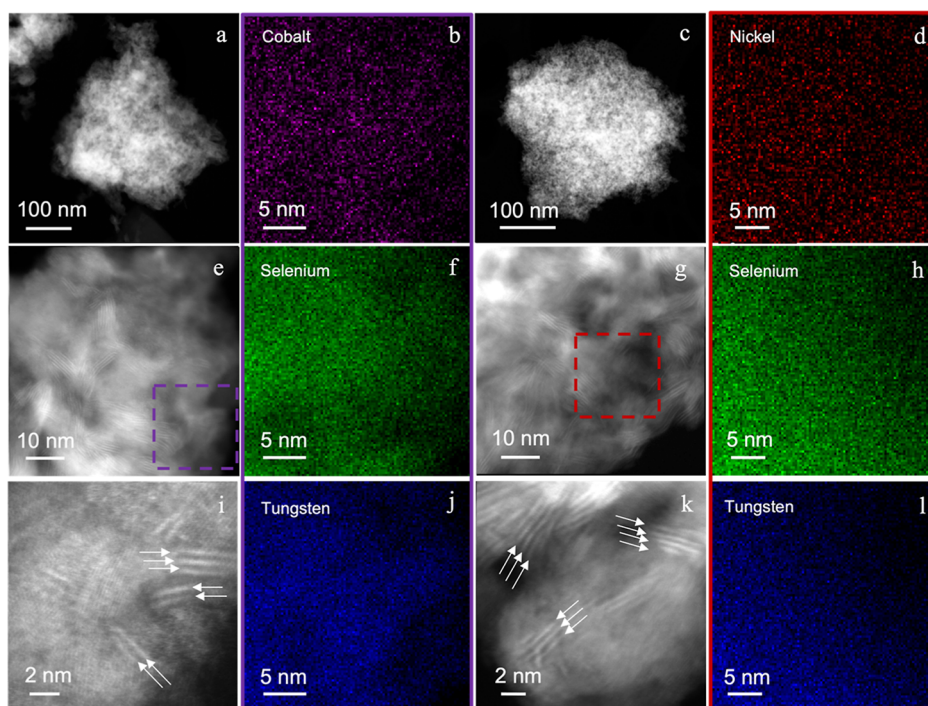


Figure 4. STEM images and STEM-EDS maps for Co-WSe₂ and Ni-WSe₂. (a,e,i) HAADF STEM images of Co-WSe₂. Lattice fringes showing the stacking of the basal planes in randomly distributed nanosheets are visible in (e,i) (indicated by arrows in (i)). The dashed window in (e) marks the area used for STEM-EDS mapping. (b,f,j) STEM-EDS maps of Co, Se, and W in Co-WSe₂, using Co-K, Se-K, and W-L EDS signals, respectively. (c,g,k) HAADF STEM images of Ni-WSe₂. Lattice fringes showing the stacking of the basal planes in randomly distributed nanosheets are visible in (g,k) (indicated by arrows in (k)). The dashed window in (g) marks the area used for STEM-EDS mapping. (d,h,l) STEM-EDS maps of Ni, Se, and W in Ni-WSe₂, using Ni-K, Se-K, and W-L EDS signals, respectively.

formation of new electronic states, which is crucial for enhancing the electrocatalytic performance of these sites.

Accordingly, Tafel slope values derived from LSV curves could provide some useful information about the HER mechanism (Figure 6b). In acidic environments, protons are first adsorbed onto the electrode surface by a reduction reaction called the Volmer step; next, molecular H₂ is produced either directly by desorption of adsorbed hydrogen atoms from the electrode, known as the Heyrovsky step, or by recombination of two adsorbed protons, called the Tafel step. Both doped materials exhibit much lower Tafel slopes of 66 mV dec⁻¹ for Ni-doped 1T/2H-WSe₂ and 88 mV dec⁻¹ for Co-doped 1T/2H-WSe₂. This would consequently mean that the desorption of adsorbed hydrogen atoms from the electrode is the rate-determining step for the former, while adsorption of protons onto the electrode surface is the rate-determining step for the latter. For comparison, the Tafel slope for pristine WSe₂ is significantly larger at 113 mV dec⁻¹, indicating poor kinetics and higher resistivity against current flow through the undoped material in 1T/2H-WSe₂.

Figure 6c illustrates the further investigation of the HER kinetics using EIS. Nyquist plots from these analyses showed that the frequency semicircle of Ni-WSe₂ is the smallest among the three, and its calculated R_{ct} is 35 Ω, whereas for Co-WSe₂, the value of R_{ct} was 66 Ω. For comparison, pristine 1T/2H-WSe₂ revealed an even higher value of the R_{ct} at 73 Ω. The smaller values of R_{ct} obtained with the doped-WSe₂ electrocatalysts indicate better conductivity and, therefore, improved electron transfer kinetics, effectively translating to the successful incorporation of atoms within 1T/2H-WSe₂.

WSe₂-doped electrocatalyst stability was then tested after 10,000 consecutive electrocatalytic cycles for both OER and HER as shown in Figures 5a and 6a, respectively. Indeed, both Co- and Ni-WSe₂ materials have demonstrated outstanding stability with only a slight negative shift in their LSV curves, as small as 20 mV after continuous cycling. Detailed electrocatalytic HER parameters are given in Table S2 for all of the tested materials.

Finally, the electrochemically active surface area (ECSA) serves as a valuable tool for gaining insights into the charge transport dynamics within doped materials. The ECSA values were calculated using the following equation: $ECSA = C_{dl}/C_s$, where C_{dl} represents the electrochemical double-layer capacitance, and C_s denotes the specific capacitance of a flat surface with 1 cm² of the real surface area, assumed to be 40 μF cm⁻² for the flat electrode. Based on this approach, cyclic voltammograms of Co- and Ni-WSe₂ along with undoped WSe₂ were recorded in a non-Faradaic region at scan rates ranging from 50 to 500 mV/s¹ (see Figure S3 in the Supporting Information). Consequently, the ECSA value for Ni-WSe₂ was found to be the highest, approximately 5.23 cm², followed by that of Co-WSe₂ with 4.75 cm². Conversely, 1T/2H-WSe₂ exhibited a lower equivalent value of approximately 1.0 cm². Typically, high ECSA values indicate a larger functional surface area of catalytic active sites, thus correlating with a better electrocatalytic performance. These findings align well with the overall electrocatalytic results. The slightly higher ECSA value for Ni-WSe₂, combined with the significantly higher atomic concentration of Co (double that of Ni) as determined by EDS analysis, likely indicates that Ni is a more efficient dopant than Co.

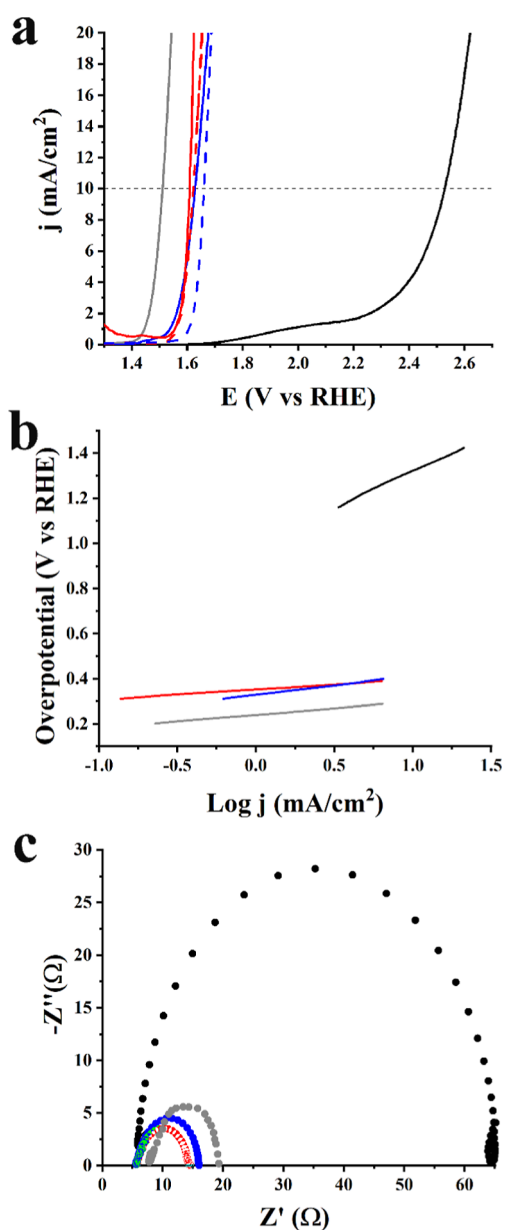


Figure 5. *iR*-corrected LSV curves for OER obtained at 1600 rpm rotation speed and 5 mV/s scan rate before (solid lines) and after 10,000 cycles (dashed lines) in aqueous 1.0 M KOH, (b) Tafel slopes and (c) Nyquist plots for Co-WSe₂ (red), Ni-WSe₂ (blue), 1T/2H-WSe₂ (black), and RuO₂ (gray).

The electrochemical performance as hydrogen evolution catalysts in polymer electrolyte membrane water electrolysis (PEMWE) cells was evaluated. Cathode electrodes were prepared with 1T/2H-WSe₂, Ni-WSe₂, Co-WSe₂, or Pt-C nanoparticles to evaluate their electrochemical activity as hydrogen evolution catalysts in a two-electrode PEMWE cell. The MEA consisted of carbon paper coated with the cathode material, titanium fiber felt coated with IrO₂ as anode catalysts, and Nafion membrane as solid electrolyte; see further details in the [Experimental Section](#). Different MEAs with an area of 4 cm² were prepared by varying only the cathode material.

[Figure 7a](#) depicts the polarization curves after the activation protocol described in the experimental section. All WSe₂-based electrocatalysts showed promising currents around 0.5–0.6 A cm⁻² at the maximum operational voltage of 2.1 V. However, it

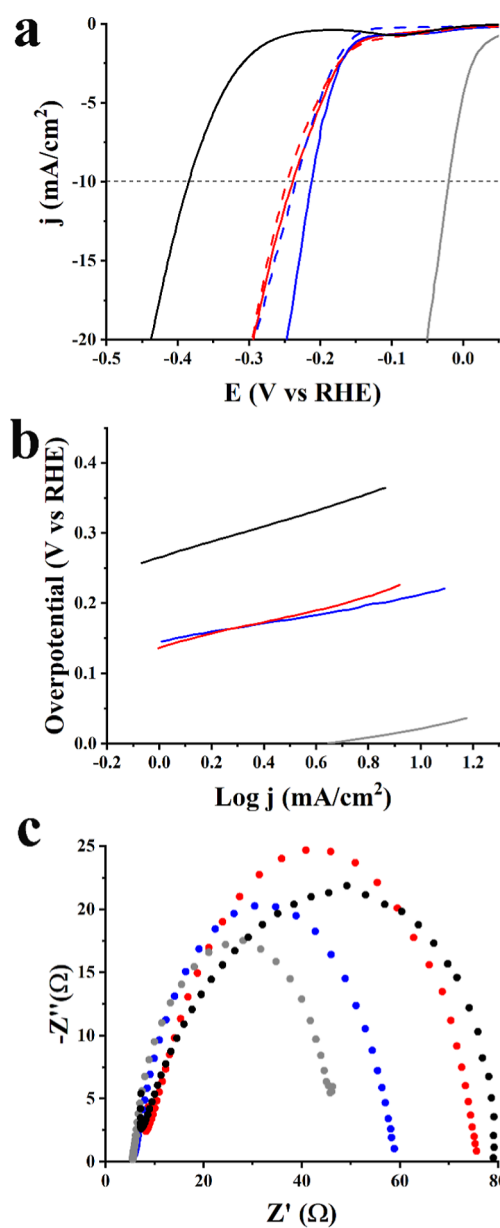


Figure 6. *iR*-corrected LSV curves for HER obtained at 1600 rpm rotation speed and 5 mV/s scan rate before (solid lines) and after 10,000 cycles (dashed lines) in aqueous 0.5 M H₂SO₄. (b) Tafel slopes and (c) Nyquist plots for Co-WSe₂ (red), Ni-WSe₂ (blue), 1T/2H-WSe₂ (black), and Pt/C (gray).

is still modest compared to the Pt-C reference cell which achieves 2.375 A cm⁻² at a similar applied bias, mainly due to a lower water splitting onset potential and better electrical conductivity. At low current density (<25 mA cm⁻²), the performance for the WSe₂-based materials is Ni-WSe₂ > Co-WSe₂ > 1T/2H-WSe₂. This is also evidenced when evaluating the reaction onset potential (graphically from the *iR*-corrected polarization curves in [Figure S3a](#)), which reveals that WSe₂ displays the worst HER activity. This is consistent with the lower charge transfer resistance obtained by EIS ([Figure 7c](#)). However, at a higher current density (>0.5 A cm⁻²), the trend changed and now the pristine WSe₂ is the best performing cathode material. This is related to the higher ohmic resistance observed in the Ni-WSe₂ and Co-WSe₂ MEAs as seen in [Figure 7b](#).

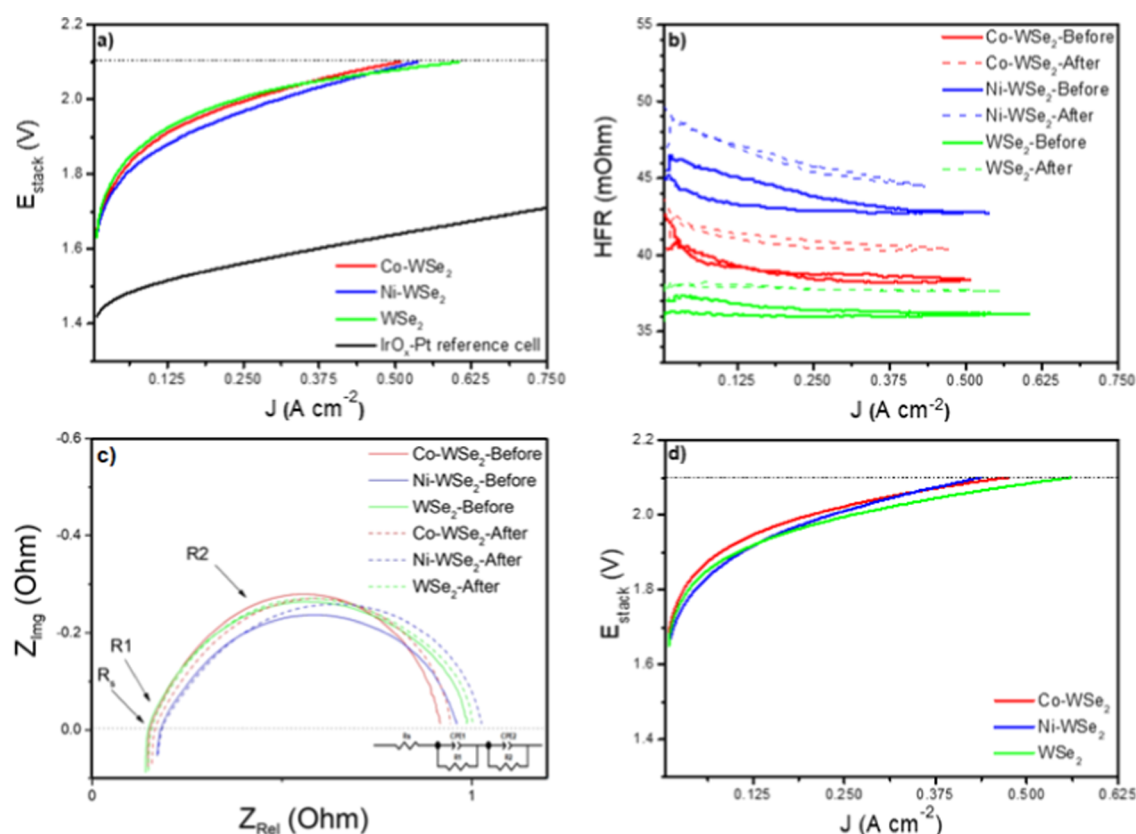


Figure 7. Galvanostatic polarization curves for MEAs prepared with the WSe_2 -based catalyst: (a) before and (d) after the stability test at 1.9 V for 24 h. (b) High-frequency response as a function of the current achieved in the potential window of 1.2–2.1 V and (c) Nyquist plots and the equivalent circuit used in the analysis of the spectra obtained from EIS at an applied current of 0.125 A/cm^2 . The label “before” and “after” refers to the initial performance and after the stability test, respectively.

Figure 7b shows the High-frequency resistance (HFR) as a function of the current which is a measurement of the Ohmic resistance in the device that considers all contributions involved, such as the characteristics of the cathode catalyst material. The HFR measurements clearly show that pristine WSe_2 has the lowest resistance values ($\sim 36 \text{ m}\Omega$) when compared to Co-WSe_2 ($\sim 39 \text{ m}\Omega$) and Ni-WSe_2 ($\sim 43 \text{ m}\Omega$). This affects the device performance by modifying the progression of the voltage with the current, observed as an increase of the curve slope. These results can be understood as follows: The doping of the $1\text{T}/2\text{H-WSe}_2$ with Co or Ni shows to improve the electrocatalytic activity of the materials, leading to a decrease in the water-splitting onset potential (relative to pristine WSe_2); however, it also modifies the particle size and morphology (as confirmed by the SEM micrographs). This consequently alters the characteristics of the catalyst layer deposited on the GDL, where the higher HFR values seen during the first polarization curve (Figure 7b, solid lines) for Ni-WSe_2 and Co-WSe_2 (compared to the undoped $1\text{T}/2\text{H-WSe}_2$) can be related to a decrease in the material conductivity or to a poor electrical contact at the cathode/membrane interface due to changes in material characteristics.

Figure 7c presents the corresponding Nyquist plots from the EIS characterization of these systems, as well as the equivalent circuit used for their fitting and calculation of the R_s (Ohmic drop resistance), R_1 (charge transfer resistance at the cathode), and R_2 (charge transfer resistance at the anode) parameters, summarized in Table S2. The R_s values agree with the HFR data, with pristine $1\text{T}/2\text{H-WSe}_2$ having the best conductivity.

On the other hand, Ni-WSe_2 exhibits the lowest R_1 values, supporting our discussion regarding the onset potential calculated graphically. Similar values were observed for the R_2 , as expected, since this represents the contribution of the anode electrode.

We also evaluated the stability of our novel WSe_2 -based catalyst by applying a constant voltage of 1.9 V for 24 h, followed by polarization curves and EIS characterization. Figure 7d presents the corresponding polarization curves where a slight decrease in the total current is observed, suggesting a minor degradation of the MEAs. The HFR increase after the stability test (Figure 7b, dashed lines) is likely caused by changes in the catalyst characteristics, such as leaching of Ni and Co. This observation is supported by the increase in the water-splitting onset potential (Figure S3b), as well as on the R_s and R_1 values (Figure 7c and Table S2). The gradual loss of the dopants can lead to reduced electrical conductivity and electrocatalytic activity. But in all cases, the Ni-WSe_2 still exhibited the best performance. The current retention for these MEAs calculated as the difference on current before and after the stability test was high, around 92.9% for the Co-WSe_2 , 81.4% for the Ni-WSe_2 , and 92.9% for the $1\text{T}/2\text{H-WSe}_2$, where the Ni-WSe_2 showed to be more susceptible to degradation than the other materials despite its high catalytic activity.

CONCLUSIONS

Due to the high energy demand, it is desirable to develop efficient electrocatalysts for water splitting and fuel-cell

technology. Aiming to improve the sluggish kinetics of the OER and reducing the cost of hydrogen fuel production by replacing costly and scarce noble metals is the ultimate goal of the commercialization of fuel cells. In the present study, Co and/or Ni atoms were introduced into 1T/2H-WSe₂ using a simple hydrothermal method and the resultant electrocatalysts were tested in water splitting. The bifunctional electrocatalysts were tested against the OER registering low overpotentials of 390 and 410 mV at 10 mA/cm² for Co- and Ni-WSe₂, respectively, due to superior reaction kinetics and charge transfer processes within the doped materials. Similar trends were obtained for the HER: Ni and Co doping of WSe₂ exhibited a low overpotential of 210 and 240 mV at -10 mA/cm², respectively. The electrocatalysts also proved to be very stable upon continuous cycling for 10,000 cycles in both reactions. From EDS analysis, Ni doping, despite its lower atomic concentration, achieves similar electrocatalytic activity to Co, highlighting its efficiency. Furthermore, the doped materials were excellent cathode electrocatalysts in a practical PEM water electrolyzer, which attained a current density of ≈600 mA/cm² at an operating potential of 2.1 V and 80 °C. The doped materials exhibited impressive operational stability by maintaining steady performance for 24 h. This straightforward preparation route, high activity, and excellent durability allow such materials to be considered as promising alternatives to noble-metal-based electrocatalysts for water splitting. In other words, this work can provide relevant guidance for further development of highly efficient, stable, and practical bifunctional electrocatalysts. By enhancing the reaction kinetics with affordable materials, our work contributes to the sustainable development of fuel cells and water-splitting technologies.

■ ASSOCIATED CONTENT

Data Availability Statement

The data sets generated during and/or analyzed during the study are accessible via the Zenodo repository: <https://zenodo.org/records/13889802>.

SI Supporting Information

The Supporting Information is available free of charge at <https://pubs.acs.org/doi/10.1021/acs.jpcc.4c08163>.

XPS spectra for Co-WSe₂ and Ni-WSe₂; table for electrocatalytic OER parameters for all tested materials; table for electrocatalytic HER parameters for all tested materials; cyclic voltammograms of WSe₂, Co-WSe₂, and Ni-WSe₂; ohmic drop polarization curves before and after the stability test for the MEAs prepared with the WSe₂-based catalyst studied in this work; and table for R_s , charger transfer resistance at the cathode (R_1), and charge transfer resistance at the anode (R_2) values extracted from the fitting of the Nyquist plots in Figure 7c before and after the stability test (PDF)

■ AUTHOR INFORMATION

Corresponding Authors

Antonia Kagkoura – Department of Inorganic Chemistry, Faculty of Chemical Technology, University of Chemistry and Technology Prague, 166 28 Prague, Czech Republic; Email: kagkourn@vscht.cz

Zdeněk Sofer – Department of Inorganic Chemistry, Faculty of Chemical Technology, University of Chemistry and Technology Prague, 166 28 Prague, Czech Republic;

orcid.org/0000-0002-1391-4448; Email: soferz@vscht.cz

Authors

Esdras J. Canto-Aguilar – Department of Physics, Umeå University, SE-901 87 Umeå, Sweden; orcid.org/0009-0003-9618-3162

Eduardo Gracia-Espino – Department of Physics, Umeå University, SE-901 87 Umeå, Sweden; orcid.org/0000-0001-9239-0541

Lunjie Zeng – Department of Physics, Chalmers University of Technology, 41296 Göteborg, Sweden; orcid.org/0000-0002-4564-7217

Eva Olsson – Department of Physics, Chalmers University of Technology, 41296 Göteborg, Sweden; orcid.org/0000-0002-3791-9569

Filipa M. Oliveira – Department of Inorganic Chemistry, Faculty of Chemical Technology, University of Chemistry and Technology Prague, 166 28 Prague, Czech Republic

Jan Luxa – Department of Inorganic Chemistry, Faculty of Chemical Technology, University of Chemistry and Technology Prague, 166 28 Prague, Czech Republic

Complete contact information is available at: <https://pubs.acs.org/10.1021/acs.jpcc.4c08163>

Notes

The authors declare no competing financial interest.

■ ACKNOWLEDGMENTS

The research leading to these results was supported by the Johannes Amos Comenius Programme, European Structural and Investment Funds, project “CHEMFELLS VI” (No. CZ.02.01.01/00/22_010/0008122) from the Ministry of Education, Youth and Sports (MEYS). Financial support from the Swedish Research Council (VR) and Swedish Foundation for Strategic Research (SSF) for the access to ARTEMI, the Swedish National Infrastructure in Advanced Electron Microscopy (2021-00171 and RIF21-0026), is also acknowledged. This work was performed in part at the Chalmers Material Analysis Laboratory, CMAL. The authors also acknowledge support from the Kempe Foundation (JCSMK 23-0095), the Carl Tryggers Foundation (CTS 21-1581), and the Swedish Foundation for Strategic Research (SSF-Agenda 2030—PUSH). Z.S. was supported by the Czech Science Foundation (GACR No. 23-05918S). This work was supported by the project “The Energy Conversion and Storage” funded as project No. CZ.02.01.01/00/22_008/0004617 by Programme Johannes Amos Comenius, call Excellent Research.

■ REFERENCES

- (1) Tan, Z. H.; Kong, X. Y.; Ng, B.-J.; Soo, H. S.; Mohamed, A. R.; Chai, S.-P. Recent Advances in Defect-Engineered Transition Metal Dichalcogenides for Enhanced Electrocatalytic Hydrogen Evolution: Perfecting Imperfections. *ACS Omega* **2023**, *8* (2), 1851–1863.
- (2) Li, S.; Zhao, Z.; Yu, D.; Zhao, J.-Z.; Su, Y.; Liu, Y.; Lin, Y.; Liu, W.; Xu, H.; Zhang, Z. Few-Layer Transition Metal Dichalcogenides (MoS₂, WS₂, and WSe₂) for Water Splitting and Degradation of Organic Pollutants: Understanding the Piezocatalytic Effect. *Nano Energy* **2019**, *66*, 104083.
- (3) Yu, M.; Budiyanoto, E.; Tüysüz, H. Principles of Water Electrolysis and Recent Progress in Cobalt-, Nickel-, and Iron-Based Oxides for the Oxygen Evolution Reaction. *Angew. Chem., Int. Ed.* **2022**, *61* (1), No. e202103824.

- (4) Fabbri, E.; Schmidt, T. J. Oxygen Evolution Reaction—The Enigma in Water Electrolysis. *ACS Catal.* **2018**, *8* (10), 9765–9774.
- (5) Ma, W.; Dong, Y.; Li, J.; Wang, Y.; Wang, T.; Zheng, X.; Deng, Y. Recent Strategies for Improving the Catalytic Activity of Ultrathin Transition Metal Sulfide Nanosheets toward the Oxygen Evolution Reaction. *Mater. Today Energy* **2024**, *40*, 101492.
- (6) Qian, Y.; Zhang, F.; Luo, X.; Zhong, Y.; Kang, D. J.; Hu, Y. Synthesis and Electrocatalytic Applications of Layer-Structured Metal Chalcogenides Composites. *Small* **2024**, *20* (26), 2310526.
- (7) Wu, W.; Tian, Q.; Jia, Y.; Xu, Q. Single-Atom Platinum Anchored on Submonolayer MoS_{2-x} for Efficient Hydrogen Evolution. *J. Phys. Chem. C* **2023**, *127* (46), 22629–22634.
- (8) Yuan, C.-Z.; Wang, S.; San Hui, K.; Wang, K.; Li, J.; Gao, H.; Zha, C.; Zhang, X.; Dinh, D. A.; Wu, X.-L.; Tang, Z.; Wan, J.; Shao, Z.; Hui, K. N. In Situ Immobilizing Atomically Dispersed Ru on Oxygen-Defective Co₃O₄ for Efficient Oxygen Evolution. *ACS Catal.* **2023**, *13* (4), 2462–2471.
- (9) Xu, J.; Ruan, J.; Jian, Y.; Lao, J.; Li, Z.; Xie, F.; Jin, Y.; Yu, X.; Lee, M.-H.; Wang, Z.; Wang, N.; Meng, H. Cobalt-Doping Induced Formation of Five-Coordinated Nickel Selenide for Enhanced Ethanol Assisted Overall Water Splitting. *Small* **2024**, *20* (11), 2305905.
- (10) Wei, T.; Liu, W.; Zhang, S.; Liu, Q.; Luo, J.; Liu, X. A Dual-Functional Bi-Doped Co₃O₄ Nanosheet Array towards High Efficiency 5-Hydroxymethylfurfural Oxidation and Hydrogen Production. *Chem. Commun.* **2023**, *59* (4), 442–445.
- (11) Man, P.; Jiang, S.; Leung, K. H.; Lai, K. H.; Guang, Z.; Chen, H.; Huang, L.; Chen, T.; Gao, S.; Peng, Y.-K.; Lee, C.-S.; Deng, Q.; Zhao, J.; Ly, T. H. Salt-Induced High-Density Vacancy-Rich 2D MoS₂ for Efficient Hydrogen Evolution. *Adv. Mater.* **2024**, *36* (17), 2304808.
- (12) Liu, L.; Liu, N.; Dai, C.; Xu, R.; Yu, G.; Wang, N.; Chen, B. MoS₂ Supported Ruthenium Nanoparticles with Abundant Sulfur Vacancies Significantly Improved Hydrogen Evolution Reaction. *Catal. Today* **2024**, *436*, 114751.
- (13) Li, B.; Wang, K.; He, S.; Du, H.; Wang, T.; Du, Z.; Ai, W. Boosted Hydrogen Evolution via Molten Salt Synthesis of Vacancy-Rich MoS_xSe_{2-x} Electrocatalysts. *ACS Sustain. Chem. Eng.* **2024**, *12* (12), 4867–4875.
- (14) Sim, Y.; Chae, Y.; Kwon, S.-Y. Recent Advances in Metallic Transition Metal Dichalcogenides as Electrocatalysts for Hydrogen Evolution Reaction. *iScience* **2022**, *25* (10), 105098.
- (15) Kagkoura, A.; Stangel, C.; Arenal, R.; Tagmatarchis, N. Molybdenum Diselenide–Manganese Porphyrin Bifunctional Electrocatalyst for the Hydrogen Evolution Reaction and Selective Hydrogen Peroxide Production. *J. Phys. Chem. C* **2022**, *126* (35), 14850–14858.
- (16) Singh, A.; Rohilla, J.; Hassan, Md. S.; C, T. D.; Ingole, P. P.; Santra, P. K.; Ghosh, D.; Sapra, S. MoSe₂/SnS Nanoheterostructures for Water Splitting. *ACS Appl. Nano Mater.* **2022**, *5* (3), 4293–4304.
- (17) Yu, W.; Zhang, S.; Gao, K.; Lin, X.; Han, Y.; Zhang, Z. Co₃O₄-MoSe₂@C Nanocomposite as a Multi-Functional Catalyst for Electrochemical Water Splitting and Lithium-Oxygen Battery. *Nanotechnology* **2022**, *33* (50), 505402.
- (18) Wei, Y.; Huang, M.; Wu, Y.; Tang, X.; Yuan, K.; Chen, Y. Selenium-Based Catalysts for Efficient Electrocatalysis. *Adv. Funct. Mater.* **2024**, *34* (42), 2404787.
- (19) Kwak, I. H.; Kim, J. Y.; Zewdie, G. M.; Yang, J.; Lee, K.-S.; Yoo, S. J.; Kwon, I. S.; Park, J.; Kang, H. S. Electrocatalytic Activation in ReSe₂-VSe₂ Alloy Nanosheets to Boost Water-Splitting Hydrogen Evolution Reaction. *Adv. Mater.* **2024**, *36* (15), 2310769.
- (20) Sun, L.; Xu, H.; Cheng, Z.; Zheng, D.; Zhou, Q.; Yang, S.; Lin, J. A Heterostructured WS₂/WSe₂ Catalyst by Heterojunction Engineering towards Boosting Hydrogen Evolution Reaction. *Chem. Eng. J.* **2022**, *443*, 136348.
- (21) Kwon, I. S.; Kwak, I. H.; Kim, J. Y.; Lee, S. J.; Sial, Q. A.; Ihsan, J.; Lee, K.-S.; Yoo, S. J.; Park, J.; Kang, H. S. 2H–2M Phase Control of WSe₂ Nanosheets by Se Enrichment Toward Enhanced Electrocatalytic Hydrogen Evolution Reaction. *Adv. Mater.* **2024**, *36* (8), 2307867.
- (22) Kagkoura, A.; Stangel, C.; Arenal, R.; Tagmatarchis, N. Molybdenum Diselenide and Tungsten Diselenide Interfacing Cobalt-Porphyrin for Electrocatalytic Hydrogen Evolution in Alkaline and Acidic Media. *Nanomaterials* **2023**, *13* (1), 35.
- (23) Li, Y.; Zhang, L.; Xiao, J.; Zhang, W. Feather-like Few-Layer WSe₂ Nanosheets Grown on W Substrates: An Excellent Electrocatalyst for the Hydrogen Evolution Reaction. *Nanoscale Adv.* **2022**, *4* (15), 3142–3148.
- (24) Muska, M.; Yang, J.; Sun, Y.; Wang, J.; Wang, Y.; Yang, Q. CoSe₂ Nanoparticles Dispersed in WSe₂ Nanosheets for Efficient Electrocatalysis and Supercapacitance Applications. *ACS Appl. Nano Mater.* **2021**, *4* (6), 5796–5807.
- (25) Cogal, S.; Celik Cogal, G.; Mičušík, M.; Kotlár, M.; Omastová, M. Cobalt-Doped WSe₂@conducting Polymer Nanostructures as Bifunctional Electrocatalysts for Overall Water Splitting. *Int. J. Hydrogen Energy* **2024**, *49*, 689–700.
- (26) Lim, J. H.; Kim, K.; Kang, J. H.; Kwon, K. C.; Jang, H. W. Tailored Two-Dimensional Transition Metal Dichalcogenides for Water Electrolysis: Doping, Defect, Phase, and Heterostructure. *ChemElectroChem* **2024**, *11* (10), No. e202300614.
- (27) Deng, Q.; Li, Z.; Huang, R.; Li, P.; Gomaa, H.; Wu, S.; An, C.; Hu, N. Research Progress of Transition-Metal Dichalcogenides for the Hydrogen Evolution Reaction. *J. Mater. Chem. A* **2023**, *11* (45), 24434–24453.
- (28) Liu, G.; Robertson, A. W.; Li, M. M.-J.; Kuo, W. C. H.; Darby, M. T.; Muhieddine, M. H.; Lin, Y.-C.; Suenaga, K.; Stamatakis, M.; Warner, J. H.; Tsang, S. C. E. MoS₂ Monolayer Catalyst Doped with Isolated Co Atoms for the Hydrodeoxygenation Reaction. *Nat. Chem.* **2017**, *9* (8), 810–816.
- (29) Yun, S. J.; Duong, D. L.; Ha, D. M.; Singh, K.; Phan, T. L.; Choi, W.; Kim, Y.-M.; Lee, Y. H. Ferromagnetic Order at Room Temperature in Monolayer WSe₂ Semiconductor via Vanadium Dopant. *Advanced Science* **2020**, *7* (9), 1903076.
- (30) Ren, Y.; Miao, X.; Zhang, J.; Lu, Q.; Chen, Y.; Fan, H.; Teng, F.; Zhai, H.; He, X.; Long, Y.; Zhang, C.; Hu, P. Post Cobalt Doping and Defect Engineering of NbSSe for Efficient Hydrogen Evolution Reaction. *J. Mater. Chem. A* **2023**, *11* (6), 2690–2697.
- (31) Presolski, S.; Wang, L.; Loo, A. H.; Ambrosi, A.; Lazar, P.; Ranc, V.; Otyepka, M.; Zboril, R.; Tomanec, O.; Ugolotti, J.; Sofer, Z.; Pumera, M. Functional Nanosheet Synthons by Covalent Modification of Transition-Metal Dichalcogenides. *Chem. Mater.* **2017**, *29* (5), 2066–2073.
- (32) Wondimu, T. H.; Bayeh, A. W.; Kabtamu, D. M.; Xu, Q.; Leung, P.; Shah, A. A. Recent Progress on Tungsten Oxide-Based Materials for the Hydrogen and Oxygen Evolution Reactions. *Int. J. Hydrogen Energy* **2022**, *47* (47), 20378–20397.
- (33) Spencer, M. A.; Holzapfel, N. P.; You, K.-E.; Mpourmpakis, G.; Augustyn, V. Participation of Electrochemically Inserted Protons in the Hydrogen Evolution Reaction on Tungsten Oxides. *Chem. Sci.* **2024**, *15* (14), 5385–5402.
- (34) Chen, J.; Chen, C.; Qin, M.; Li, B.; Lin, B.; Mao, Q.; Yang, H.; Liu, B.; Wang, Y. Reversible Hydrogen Spillover in Ru-WO_{3-x} Enhances Hydrogen Evolution Activity in Neutral PH Water Splitting. *Nat. Commun.* **2022**, *13* (1), 5382.
- (35) Chen, X.; Yang, J.; Cao, Y.; Kong, L.; Huang, J. Design Principles for Tungsten Oxide Electrocatalysts for Water Splitting. *ChemElectroChem* **2021**, *8* (23), 4427–4440.
- (36) Zhang, R.; Drysdale, D.; Koutsos, V.; Cheung, R. Controlled Layer Thinning and P-Type Doping of WSe₂ by Vapor XeF₂. *Adv. Funct. Mater.* **2017**, *27* (41), 1702455.
- (37) Tan, X.; Zhao, D.; Sun, Y.; Duan, Z.; Wang, X.; Wu, X. Co-Doped MoS₂ Nanosheet: A Stable and PH-Universal Electrocatalyst for an Efficient Hydrogen Evolution Reaction. *CrystEngComm* **2022**, *24* (38), 6696–6704.
- (38) Wang, G.; Zhang, G.; Ke, X.; Chen, X.; Chen, X.; Wang, Y.; Huang, G.; Dong, J.; Chu, S.; Sui, M. Direct Synthesis of Stable 1T-MoS₂ Doped with Ni Single Atoms for Water Splitting in Alkaline Media. *Small* **2022**, *18* (16), 2107238.

(39) Karthikeyan, R.; Thangaraju, D.; Prakash, N.; Hayakawa, Y. Single-Step Synthesis and Catalytic Activity of Structure-Controlled Nickel Sulfide Nanoparticles. *CrystEngComm* **2015**, *17* (29), 5431–5439.

(40) Wen, X.; Feng, W.; Li, X.; Yang, J.; Du, R.; Wang, P.; Li, H.; Song, L.; Wang, Y.; Cheng, M.; He, J.; Shi, J. Diatomite-Templated Synthesis of Single-Atom Cobalt-Doped MoS₂/Carbon Composites to Boost Sodium Storage. *Adv. Mater.* **2023**, *35* (36), 2211690.

(41) Liu, Z.; Nie, K.; Qu, X.; Li, X.; Li, B.; Yuan, Y.; Chong, S.; Liu, P.; Li, Y.; Yin, Z.; Huang, W. General Bottom-Up Colloidal Synthesis of Nano-Monolayer Transition-Metal Dichalcogenides with High 1T'-Phase Purity. *J. Am. Chem. Soc.* **2022**, *144* (11), 4863–4873.

(42) Kagkoura, A.; Wei, S.; Zeng, L.; Olsson, E.; Oliveira, F. M.; Luxa, J.; Sofer, Z. Mn-Doped WSe₂ as an Efficient Electrocatalyst for Hydrogen Production and as Anode Material for Lithium-Ion Batteries. *Nanoscale* **2025**, *17* (2), 947–954.